ELSEVIER

Journal of the Mechanics and Physics of Solids
51 (2003) 2191–2211

JOURNAL OF THE
MECHANICS AND
PHYSICS OF SOLIDS

www.elsevier.com/locate/jmps

Measurement of full-field curvature and geometrical instability of thin film-substrate systems through CGS interferometry

T.-S. Park[a], S. Suresh[a], A.J. Rosakis[b,*], J. Ryu[c]

[a] *Department of Materials Science and Engineering, Massachusetts Institute of Technology, Cambridge, MA 02139, USA*

[b] *Graduate Aeronautical Laboratories, California Institute of Technology, Pasadena, CA 91125, USA*

[c] *Department of Electrical Engineering and Computer Science, Massachusetts Institute of Technology, Cambridge, MA 02139, USA*

Abstract

Large deformation behavior prior to and after bifurcation of thin W films on much thicker Si substrates is investigated by recourse to coherent gradient sensing (CGS), which is an optical, full-field and vibration-insensitive technique. Since fringes obtained by CGS represent the contours of gradient in out-of-plane displacement through appropriate optics, curvature of the wafer can be obtained directly from the fringe number density. The measured curvatures in two orthogonal principal directions, whose values agree reasonably with both analytical and numerical predictions based on large deformation theory, clearly show that the equilibrium shape of the wafer changes from a sphere to an ellipsoid when bifurcation occurs. In contrast to the one-dimensional scanning method, which provides only a single normal (or direct) curvature component, twist (or shear) as well as normal components of curvatures can be obtained as the wafer is rotated with respect to its flat zone. A classical Mohr's circle representation is also used to rationalize evolution of the twist curvatures. Finally, local curvature variations due to non-uniform film stresses can be captured by full-field curvature maps using image processing analysis.

Keywords: Bifurcation; Coherent gradient sensing; Full-field curvature map; Large deformation; Twist curvature

* Corresponding author. Tel.: +1-626-395-4523; fax: +1-626-449-6359.
E-mail address: rosakis@aero.caltech.edu (A.J. Rosakis).

0022-5096/$ - see front matter © 2003 Elsevier Ltd. All rights reserved.
doi:10.1016/j.jmps.2003.09.031

1. Introduction

The drive for miniaturization and more efficient computer chip manufacturing has motivated the microelectronic industry to fabricate increasingly large Si wafers on which a greater number of dies could be fabricated. At the turn of the century, the semiconductor industry is in the midst of retooling its wafer fabrication facilities to handle 300-mm (12-in) diameter Si wafers, instead of the current standard, 200-mm wafers. This increase in wafer diameter is also accompanied by a growing trend to introduce more levels of metallization on the Si substrate which, in turn, results in a higher effective membrane force in the multi-level, thin film arrangement on the substrate. Trends in the fabrication of copper metal interconnects using the Damascene process also involve the so-called chemical–mechanical polishing (CMP) method whereby planarization is achieved between different metallization steps. Finally, Si wafer substrate thicknesses are becoming progressively smaller driven by packaging level needs. The collective effect of these trends in computer chip manufacturing is that while the propensity for inducing large (or non-linear) deformation in the substrate is significantly enhanced, there is also growing need to ensure that wafer surfaces remain planar during different stages of manufacturing.

Dimensional analysis and computational modeling of large deformation indicate that the propensity for bifurcation is proportional to the mismatch stress in the film (σ_f), the film thickness (h_f) and the square of the substrate diameter (D_s^2), and inversely proportional to h_s^3, where h_s is the thickness of the substrate (Salamon and Masters, 1995; Finot and Suresh, 1996; Finot et al., 1997; Freund, 2000). Another way of viewing this is to observe that this propensity is directly proportional to two non-dimensional ratios of lengths in addition to being proportional to the film stress. These are (h_f/h_s) and $(D_s/h_s)^2$. The first is the thickness ratio of the film to the substrate while the second is the wafer aspect ratio. These dimensional considerations for large deformation also suggest that for fixed substrate diameter, film mismatch stress and film thickness, there exists a critical thickness of the substrate above which curvature bifurcation is suppressed (Finot et al., 1997). Similarly, different combinations of substrate geometry and film membrane force, $\sigma_f \times h_f$, for which non-linear elastic deformation is suppressed can also be identified (Finot et al., 1997). When a wafer undergoes large deformation, a biaxial curvature state develops and curvatures may no longer be uniform over the entire wafer even with uniform film membrane force (Finot et al., 1997; Freund, 2000). The details of the non-linear deformation states and the location of bifurcation point strongly depend on gravity as well as arrangement of supporting points (Giannakopoulos et al., 2001). In-plane shape of the film–substrate system also influences the onset of instability. For example, rectangular shape leads to more gradual transition from spherical to ellipsoidal curvature, whereas circles and squares lead to a sharp bifurcation point (Finot and Suresh, 1996; Giannakopoulos et al., 2001).

Large deformation and bifurcation have been observed with different curvature measurement techniques. Finot et al. (1997) investigated thin W films on 150-mm (6-in) and 200-mm (8-in) diameter Si wafers, the backsides of which were polished to induce large deformation. Non-uniform curvature values were measured along the wafer

diameter over a range of film membrane forces and substrate geometries with the laser scanning method. An advantage of the laser scanning method lies in its good sensitivity (Pan and Blech, 1984). However, the laser scanning technique provides point-wise information and could potentially miss localized anomalies. Even if complete curvature maps were generated by scanning, these scans would reveal only one of the three independent components of the curvature tensor.

The grid reflection technique, which projects a grid on the surface of wafers, and then collects a reflected image containing information on the out-of-plane displacement of the surface, was also employed to study bifurcation behavior (Finot et al., 1997; Giannakopoulos et al., 2001). The grid reflection provides full-field measurement over the entire wafer, and can capture clear transition between before and after bifurcation from the distortion of grid shape. The multi-beam optical stress sensor technique (Floro and Chason, 1996) is another optical technique which exploits the advantages of a multi-beam output. However, this technique has not been used for measuring large diameter wafers due to its limited field-of-view.

The coherent gradient sensing (CGS) technique (Rosakis et al., 1998), which obtains gradient in the out-of-plane displacement of the wafer surface was also used for investigation of non-linear deformation (Lee et al., 2001). Techniques based on optical interferometry offer much promise as a means for real-time, non-intrusive, full-field measurement of curvature changes. However, standard interferometric techniques, such as Twyman–Green interferometry (Born and Wolf, 1986), are sensitive to rigid body motion (translation and/or rotation), and therefore are very vibration-sensitive. Moreover, since these interferometric techniques measure the surface topography, two successive differentiations of the experimental data are required to obtain curvature components. Since the CGS technique measures gradient of displacements on the specimen surface, this technique is vibration-insensitive and requires only one differentiation of the experimental data to get curvature field. Lee et al. (2001) studied deviation from linear prediction in Al films on 50-mm (2-in) diameter, ultra thin (105 μm) Si wafers during thermal cycling using the CGS technique. Full-field observation of the entire wafer was performed from different wafer rotations, but only radial curvatures were calculated prior to and after bifurcation in comparison with finite element simulations. No attempt was made to visualize the twist curvature states during this process.

In this work, non-linear deformation of back-side polished, 150-mm (6-in) Si wafers coated with thin W films, which are purely elastic and elastically isotropic, were investigated using the CGS technique. First, curvatures in two orthogonal, principal directions were compared with analytical and numerical predictions in non-linear deformation range. Because of CGS' two-dimensional capability, twist (shear) curvature components as well as both normal curvature components of the wafer were measured in the off-principal directions as a function of wafer rotation. A classical Mohr's circle representation was used to rationalize normal and twist curvature variation with rotation angles. Finally, full-field curvature maps were constructed from CGS fringe patterns using an image processing technique for non-uniform curvature fields resulting from local stress variation.

2. Theoretical background

2.1. Curvature analysis based on large deformation theory

The curvature of a substrate coated with a thin film in an equibiaxial stress state is linearly proportional to the membrane force, $\sigma_f \times h_f$, and is given by Stoney (1909) as

$$\kappa_{\text{Stoney}} = \frac{6}{\overline{E_s}} \frac{\sigma_f h_f}{h_s^2}, \tag{1}$$

where $\overline{E_s}$ is the biaxial modulus ($E_s/[1-\nu_s]$) of the substrate. Since this relation is based on small deformation theory assuming small rotations, there is no dependence on lateral dimensions such as substrate diameter. When out-of-plane displacement is comparable to substrate thickness, however, large deformation theory, which take moderate rotation into account, should be used to capture actual curvature changes of the thin film–substrate structure.

In order to evaluate quantitatively the significance of large deformation, it is convenient to introduce a stress parameter, A, defined (Finot et al., 1997) as

$$A = (\sigma_f h_f) \cdot \left(\frac{D_s^2}{h_s^3}\right) = \sigma_f \cdot \left(\frac{h_f}{h_s}\right) \cdot \left(\frac{D_s}{h_s}\right)^2. \tag{2}$$

The parameter A, which primarily controls the extent of large deformation, also provides a geometrical interpretation in that it is proportional to the ratio of the out-of-plane deflection at the edge of the wafer to the wafer thickness. It is known that bifurcation and geometrical instability of a circular wafer coated with a thin film occur at a critical value of the stress parameter, A_c (Salamon and Masters, 1995; Finot and Suresh, 1996). For $D_s/h_s \geqslant 50$, A_c depends only on the mechanical properties of the substrate, and full-field finite element analysis gives $A_c = 680$ GPa for a Si substrate (Finot et al., 1997).

Fig. 1 shows the variation of curvature κ at the center of the wafer from numerical simulation, normalized by the predicted small deformation curvature κ_{Stoney}, as a function of the parameter A, normalized by its critical value A_c at bifurcation (Finot et al., 1997). There are three distinct regimes which mark clear transitions in the evolution of curvature. For low values of A/A_c, the stresses in the film promote only small deformation with the result that the Stoney formula, Eq. (1), adequately describes the evolution of the spherical curvature. Specifically when $A/A_c \leqslant 0.2$ (regime I), the curvature of the wafer predicted from the finite element analysis, κ, deviates by less than 10% from the small deformation approximation. In regime I, the two direct curvature components are equal and are uniform along the entire wafer. The curvature tensor is isotropic and the twist vanishes in any reference axis.

When $0.2 \leqslant A/A_c \leqslant 1.0$ (regime II), the radially symmetric shape of the film–substrate system is retained. However, the wafer is no longer a sphere and it assumes a frisbee-like shape. At the center of the wafer, the large deformation of the bilayer leads to a

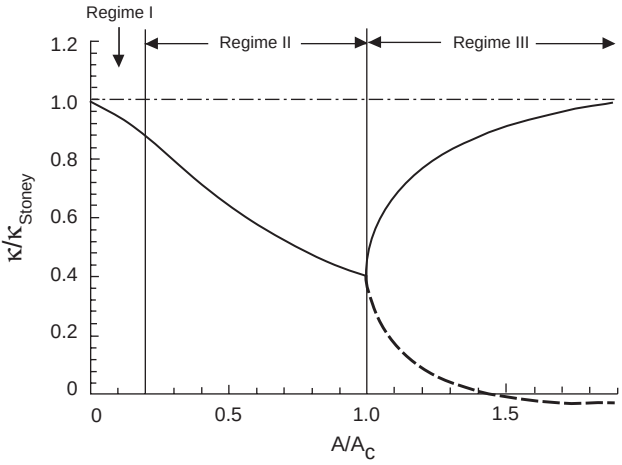

Fig. 1. Numerical predictions of principal curvatures at wafer center normalized by the small deformation spherical curvature (κ_{Stoney}) as a function of the ratio A/A_c.

non-linear relationship between the curvature, κ, and the membrane force, $\sigma_f \times h_f$. Consequently, the numerical values of κ deviate markedly from the Stoney prediction (Stoney formula underestimates film stress). In addition, the curvature is not uniform across the wafer and the radial variation of the curvature between the center of the wafer and the edge is larger than 10%, even with uniform membrane force. This variation was investigated experimentally by Finot et al. (1997) and Lee et al. (2001) using two different optical methods.

When the value of A approaches A_c, bifurcation occurs in the curvature of the film–substrate system, and the layered solid undergoes an abrupt shape change from a spherical geometry to an ellipsoidal shape. For $A/A_c \geqslant 1$ (regime III), this ellipsoidal shape leads to a large curvature, κ_x, in one direction and a smaller curvature, κ_y, in the in-plane orthogonal direction. As A/A_c increases, κ_y goes to zero and the wafer consequently becomes cylindrical.

This curvature bifurcation phenomenon arises from the fact that the substrate cannot deform into a spherical cap shape without stretching or compressing portions of its midplane when deformation is not small. The substrate is very stiff in extension compared to bending due to its plate-like shape. Therefore, this coupling between curvature and stretching tend to stiffen the system response in comparison with behavior in the linear range (regime II) (Freund, 2000; Freund and Suresh, 2003). Furthermore, in contrast to spherical bending, ellipsoidal (or cylindrical) bending can occur with only very limited midplane extension, which suggests that the system may begin a transition at some critical stress parameter (A_c) from axially symmetric deformation, as the only possible equilibrium shape, toward cylindrical bending deformation as an alternate shape, which is energetically favorable (regime III) (Salamon and Masters, 1995; Freund and Suresh, 2003).

2.2. Mohr's circle representation of curvature

For displacements associated with the evolution of deformation at a point on an initially planar surface, the components of curvature can be generally non-linear functions of the orthogonal displacement components at that point and their derivatives with respect to the spatial coordinate (say x, y). Each of the curvature components depend on the orientation of the coordinate system with reference to the surface. For deformed surfaces where the squares of the slopes are small compared to unity (Rosakis et al., 1998; Freund and Suresh, 2003),[1] the components of curvature can be defined in a simplified form as (Hyer, 1981; Rosakis et al., 1998)

$$\kappa_x = \frac{\partial^2 f}{\partial x^2}, \quad \kappa_y = \frac{\partial^2 f}{\partial y^2}, \quad \kappa_{xy} = \frac{\partial^2 f}{\partial x \partial y}, \quad \kappa_{yx} = \frac{\partial^2 f}{\partial y \partial x}, \tag{3}$$

where $z = f(x, y)$ is the equation of the deformed surface topography induced by the out-of-plane displacement. The first two equations define two direct (or normal) curvatures along two arbitrarily chosen, but mutually orthogonal directions, x and y. They represent the rate of change in slope along the direction of travel per unit distance (either x or y). The third and fourth equations define the twist (or shear) curvatures. These are defined as the rate of change in slope perpendicular to the direction of travel. Because of the interchangeability of the differentiation operation, $\kappa_{xy} = \kappa_{yx}$ and as a result, curvature at a point is completely defined by the three independent measures κ_x, κ_y and κ_{xy}.

The situation is analogous to a two dimensional state of plane stress in a thin body subjected to external in-plane forces and undergoing planar deformations. The stress state in such a case is defined by two direct in-plane stresses and an in-plane shear stress, which are only surviving components of the symmetric stress tensor. Similar to this, the curvature at a point on a surface is also a symmetric tensor whose components are κ_x, κ_y and κ_{xy} with respect to an arbitrarily chosen cartesian coordinate system (x, y, z), whose x–y plane serves as the reference plane from which the topography of $z = f(x, y)$ of the surface is measured.

The symmetry of the curvature tensor ensures the existence of at least two mutually perpendicular directions, defined at each point, along which one of the normal curvatures is maximized while the other is minimized. Along these directions, called principal directions, the twist curvatures vanish. These maximum and minimum curvatures are called the principal curvatures and will be denoted as κ_1 and κ_2, respectively. Along two directions inclined at $+45°$ and at $-45°$ to the principal directions, the twist curvatures are maximized while the two normal curvatures become equal and are given by $(\kappa_x + \kappa_y)/2$. Each point on the curved surface features principal directions that are inclined at different directions to, the initially chosen, x–y axes. The principal curvatures also vary from point to point. For spherically deformed surfaces, the curvature tensor is isotropic and two normal curvatures are equal to each other and remain

[1] It should be noted that strains are still small, even when second-order contribution of rotation to strain can be as significant as the first-order linear term in non-linear deformation.

constant from point to point. In this case, any direction is a principal direction and the shear or twist curvatures vanish everywhere.

In stress analysis, Mohr's circle offers a convenient method of visualizing the state of plane stress and of extracting, from simple geometrical conditions, normal and shear stresses and directions of principal stresses. Similarly, it will be shown in the present discussion that Mohr's circle can be constructed to determine different components of curvature at any point on a deformed surface and to visualize principal directions and curvatures.

The Mohr's circle for curvature is drawn with κ_x and κ_y plotted as variables along the abscissa and κ_{xy} plotted along the ordinate, as shown in Fig. 2 (Hyer, 1981; Finot and Suresh, 1996). The center of the Mohr's circle, located along the abscissa at the value, C_{Mohr}, and its radius, R_{Mohr}, are given, respectively, by

$$C_{\text{Mohr}} = \frac{\kappa_x + \kappa_y}{2}, \quad R_{\text{Mohr}} = \left\{ \left(\frac{\kappa_x - \kappa_y}{2} \right)^2 + \kappa_{xy}^2 \right\}^{1/2}. \tag{4}$$

The principal curvatures for the surface, representing the maximum and minimum values of normal curvatures, are then simply given by

$$\kappa_1 = C_{\text{Mohr}} + R_{\text{Mohr}}, \quad \kappa_2 = C_{\text{Mohr}} - R_{\text{Mohr}}. \tag{5}$$

The principal curvatures are found at directions θ and $\theta + 90°$, where

$$\tan 2\theta = \frac{2\kappa_{xy}}{\kappa_x - \kappa_y}. \tag{6}$$

In other words, θ is the angle through which the coordinate system should be rotated counterclockwise about the z-axis (looking toward the x–y plane along the z-direction) in order to align the x- and y-axis with the principal curvatures, κ_1 and κ_2. Mohr's circle can be used to determine which of these two axes is aligned with κ_1 or κ_2.

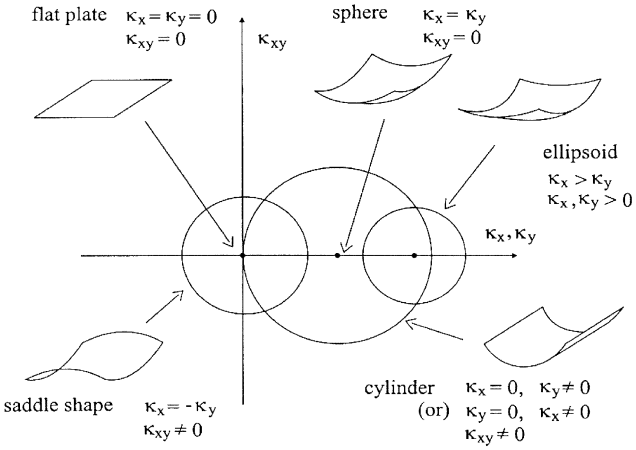

Fig. 2. Mohr's circle representation of the shapes of curved surfaces (From Finot and Suresh, 1996).

Whereas the twist curvature vanishes in the principal curvature directions, maximum twist curvature κ_{12} occurs at orientations $\theta \pm 45°$ and is given by

$$\kappa_{12} = \frac{\kappa_1 - \kappa_2}{2} = R_{\text{Mohr}}. \tag{7}$$

Different shapes of curved surfaces are easily visualized using the Mohr's circle, as shown in Fig. 2. For a flat surface with no curvature, $\kappa_x = \kappa_y = \kappa_{xy} = 0$, and the Mohr's circle reduces to a point located at the origin of the κ_x/κ_y versus κ_{xy} plot. For spherically curved surfaces, the Mohr's circle is a point located along the abscissa. For a cylindrical surface, either κ_x or κ_y vanishes and the Mohr's circle has its left or right extreme coincident with the origin of the curvature plot. For a saddle-shaped surface, the Mohr's circle encloses the origin.

3. Experiment and analysis

3.1. CGS Interferometry

Two Si wafers with 150-mm diameter, 675 μm initial thickness, and (100) surface orientation were prepared for this study. In order to induce different extents of large deformation, the wafers were ground and polished from the back side. The effect of residual stress in the silicon due to grinding and polishing is known to be negligible (Finot et al., 1997). The film–substrate geometries discussed here include a 325 μm thick substrate with a 0.9 μm thick W film (wafer A) and a 415 μm thick substrate with a 2.4 μm thick W film (wafer B). Curvatures were measured by CGS interferometry for both wafers and compared with the previous experimental results of the same specimens using the laser scanning and grid reflection methods (Finot et al., 1997). Numerical simulations were forced to match the measured curvatures (at the center region) to extract membrane forces in the films from the fit (Finot et al., 1997). Measured curvatures were plotted as a function of corresponding membrane forces in the principal directions for comparison with theoretical prediction, which will be discussed in the following section. CGS interferograms were also taken at every 45° with respect to the flat zones of the wafers by rotating the entire wafers at a fixed experimental condition for the purpose of investigating twist curvature evolution in the off-principal directions.

Fig. 3 shows a schematic of the CGS setup in reflection (Rosakis et al., 1998; Lee et al., 2001). A coherent, collimated laser beam is directed to the specularly reflecting specimen surface via a beam splitter. The beam reflected from the specimen then passes through the beam splitter and is then incident upon a pair of identical high-density (40 lines/mm) gratings, G_1 and G_2, separated by a distance, Δ (40 mm in this experiment). The diffracted orders from the two gratings are spatially filtered using a filtering lens to form distinct diffraction spots on the filter plane. An aperture placed in this plane serves to filter out the diffraction order of interest, which is then imaged onto the photographic film plane. For the present purpose, either of the ± 1 diffraction orders is of interest, as will be clear in the following discussion.

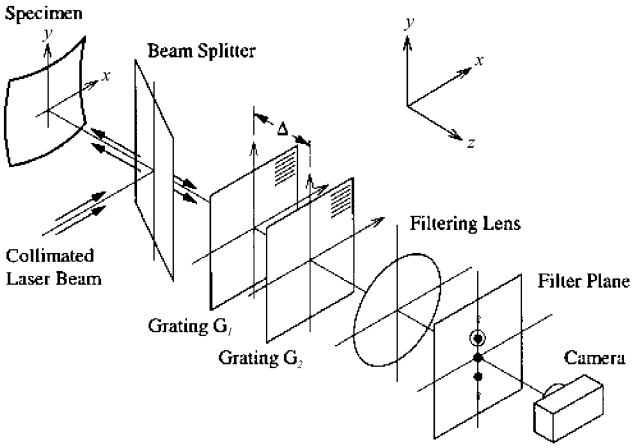

Fig. 3. Schematic of the CGS set up in reflection mode (From Rosakis et al., 1998).

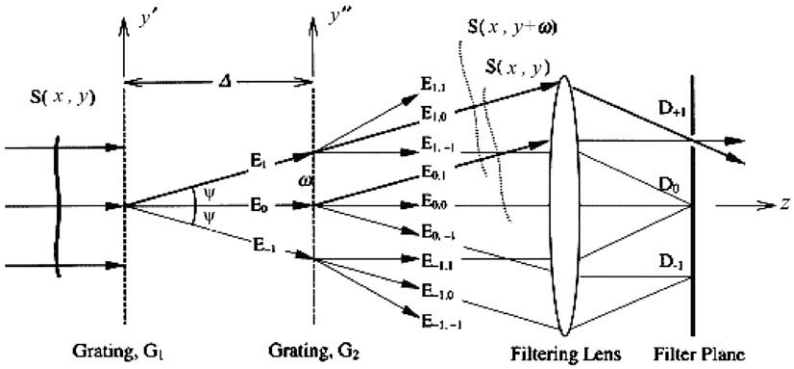

Fig. 4. Schematic to illustrate the working principle of CGS (From Rosakis et al., 1998).

Fig. 4 illustrates the working principle of CGS in two dimensions (Rosakis et al., 1998). Consider an optical wave front, $S(x, y)$, reflected from the specimen, which is directly related to out-of-plane displacement, $f(x, y)$, via the relation

$$S(x, y) = 2f(x, y) \tag{8}$$

A wave front incident on the primary grating, G_1, is diffracted into several wave fronts denoted as $E_0, E_1, E_{-1}, E_2, E_{-2}$, etc. For illustrative purposes, only E_0, E_1, E_{-1} are shown in Fig. 4. Each of these wave fronts are further diffracted by the second grating, G_2, to give rise to wave fronts denoted as $E_{0,0}, E_{0,1}, E_{0,-1}, \ldots, E_{1,0}, E_{1,1}, E_{1,-1}, \ldots, E_{-1,0}, E_{-1,1}, E_{-1,-1}$, etc. Again, only some of the diffracted wave fronts are shown. Now various sets of parallel diffracted beams are combined using the filtering lens to form diffraction spots $D_0, D_1, D_{-1}, \ldots$ in the filter plane which coincides with

the focal plane of the lens. An aperture is placed on the filter plane to block all but the D_{+1} diffraction spot. Subsequently, this diffraction spot is imaged onto the film plane.

Assume that the optical wave front incident on the first grating, G_1, is approximately planar and has a local phase difference given as $S(x, y)$. Consider only two diffracted wave fronts, $E_{1,0}$ and $E_{0,1}$. For $E_{1,0}$, it is diffracted at the first grating and transmitted without diffraction at the second. For $E_{0,1}$, it is transmitted at the first grating and is diffracted at the second. Since both wave fronts undergo one transmission and one diffraction, these wave fronts should be coherent, i.e. in the same phase. The net effect of the two gratings is to produce a lateral shift, or shearing, of the incident wave front. Thus the optical wave front along the diffracted beam $E_{1,0}$, given by $S(x, y + \omega)$, is shifted by an amount ω along the y-direction as compared to the wave front along the diffracted beam $E_{0,1}$, given by $S(x, y)$. The wave front shift is parallel to the principal axis of the gratings, i.e. along y-direction, if the grating lines are oriented along the x-direction as shown in Fig. 4.

Moreover, the magnitude of the shift is a function of the grating separation Δ and the diffraction angle ψ as

$$\omega = \Delta \tan \psi, \tag{9}$$

where the diffraction angle, ψ, is given by

$$\psi = \arcsin(\lambda / p), \tag{10}$$

with λ being the wavelength of light and p being the grating pitch. For a small angle of diffraction, Eqs. (9) and (10) approximate to

$$\omega \approx \Delta \psi, \tag{11}$$

$$\psi \approx \frac{\lambda}{p}. \tag{12}$$

Now consider the interference of the wave fronts. The conditions for constructive interference may be expressed as

$$S(x, y + \omega) - S(x, y) = n^{(y)} \lambda, \quad n^{(y)} = 0, \quad \pm 1, \pm 2, \ldots, \tag{13}$$

where $n^{(y)}$ represents the integer identifying fringes observed for shearing along the y-direction. Dividing Eq. (13) by ω gives

$$\frac{S(x, y + \omega) - S(x, y)}{\omega} = \frac{n^{(y)} \lambda}{\omega}, \quad n^{(y)} = 0, \quad \pm 1, \pm 2, \ldots \tag{14}$$

which, for sufficiently small ω, may be approximated by

$$\frac{\partial S(x, y)}{\partial y} = \frac{n^{(y)} \lambda}{\omega}, \quad n^{(y)} = 0, \pm 1, \pm 2, \ldots \ . \tag{15}$$

Using Eqs. (11) and (12) in Eq. (15), we have

$$\frac{\partial S(x,y)}{\partial y} = \frac{n^{(y)}p}{\Delta}, \quad n^{(y)} = 0, \pm 1, \pm 2, \dots \ . \tag{16}$$

Generalizing the result to include wave front shearing in either the x- or y-direction, we have

$$\frac{\partial S(x,y)}{\partial \alpha} = \frac{n^{(\alpha)}p}{\Delta}, \quad n^{(\alpha)} = 0, \pm 1, \pm 2, \dots, \tag{17}$$

where n^{α} represents the fringes observed for shearing along the α-direction and $\alpha \in \{x, y\}$. Eq. (17) is the governing equation for interferograms formed using the technique of CGS.

Symmetric curvature tensor, $\kappa_{\alpha\beta}$, where $\alpha, \beta \in \{x, y\}$, has components κ_{xx} (or κ_x) and κ_{yy} (or κ_y) termed as the normal curvatures and κ_{xy} termed as the twist curvatures as described in detail in Section 2.2. The principal values of $\kappa_{\alpha\beta}$ are termed as the principal curvatures. When $|\nabla f|^2 \ll 1$, which is strictly valid even in large deformation regime (Freund, 2000; Freund and Suresh, 2003), curvatures can be expressed combining Eq. (8) as

$$\kappa_{\alpha\beta} \approx \frac{\partial^2 f(x,y)}{\partial\alpha\partial\beta} \approx \frac{p}{2\Delta}\left(\frac{\partial n^{(\alpha)}(x,y)}{\partial\beta}\right), \quad n^{(\alpha)} = 0, \pm 1, \pm 2, \dots \ , \tag{18}$$

where $\alpha \in \{x, y\}$. Eq. (18) is the principal governing equation for determining curvature tensor fields, $\kappa_{\alpha\beta}(x, y)$, where $\alpha, \beta \in \{x, y\}$, from CGS interferograms. In this manner, CGS interferograms provide a full-field technique for determining the instantaneous value of the specimen curvature tensor at any point (x, y). Moreover, since CGS technique provides the out-of-plane gradient of the specimen surface topography, it is not sensitive to rigid body motion such as vibration. In addition, only one differentiation of the experimental data is required to obtain curvature since the CGS interferogram is already differentiated once by optical means.

3.2. Image processing analysis

After obtaining two independent out-of-plane displacement gradient fields by the CGS technique, numerical differentiation of these fields follows via a commercial MATLAB program (MATLAB Version 6.1, 2001) to construct three full-field curvature (MATLAB Version 6.1, 2001) to construct three full-field curvature component maps (see Eq. (3)). Fig. 5(a) shows a slope interferogram ($\partial f/\partial y$, in this case) from a 52-mm diameter region near the center of a W film on a Si substrate. Change in fringe density across the field of view encodes the curvature variation of the surface. Digital image processing techniques are used to obtain a map of fringe density from the interferogram automatically. This is achieved as follows:

The first step is to represent dark regions of the fringes in Fig. 5(a) by a set of lines of single pixel width, as shown in Fig. 5(b). A thresholding technique is subsequently used to group the pixels comprising the interferogram into two subgroups, depending on their brightness values. Through this thresholding technique, the dark regions in

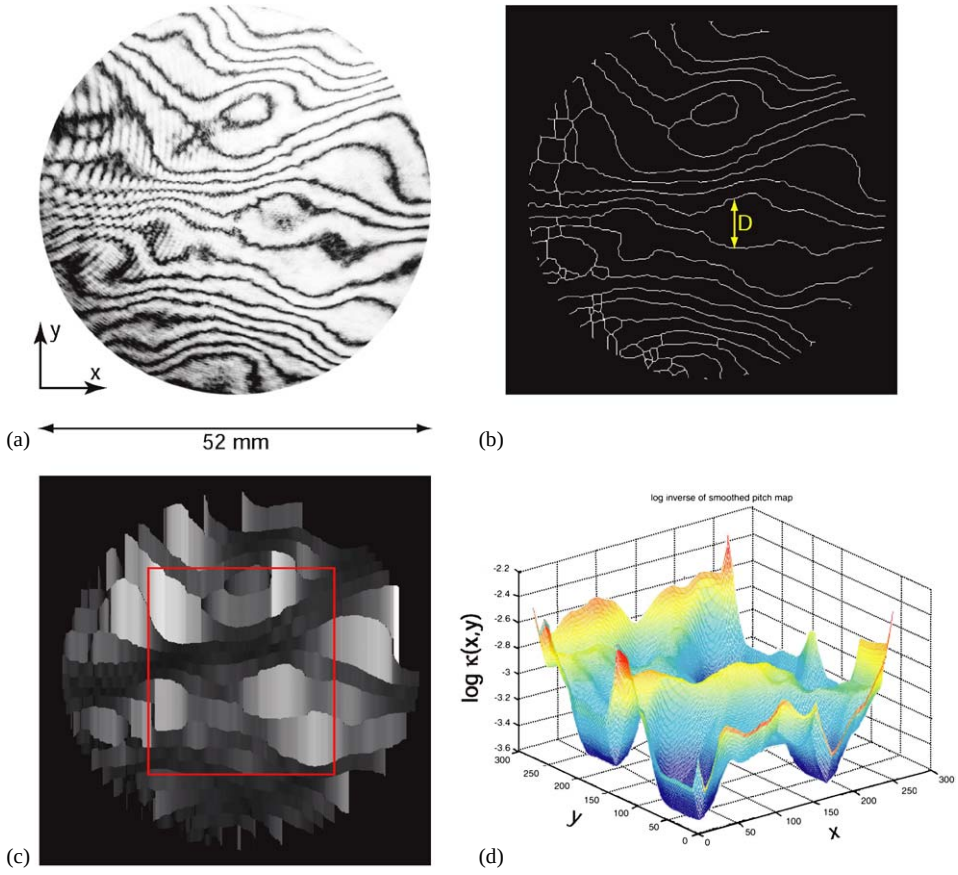

Fig. 5. Image processing procedure from a CGS interferogram to a full-field curvature map (a) an interferogram of a 52-mm diameter region of the wafer using CGS method. (On the left side, there exist secondary, spherical fringes on top of the main fringes. These fringes are artifacts from the laser beam, and are not generated by wafer curvature.) (b) a binary image in which the dark fringes in (a) are represented by lines with one pixel width. (c) a gray scale map of pitch (or spacing), determined by estimating vertical distances between adjacent lines in (b). (d) a curvature map on a logarithmic scale of the rectangular region in (c) obtained using Eq. (18) (0.1 mm per pixel).

Fig. 5(a) take the value of one in a binary image, i.e. full brightness. A series of morphological processing algorithms is then applied to obtain the final image shown in Fig. 5(b).

A local pitch (or spacing) map is constructed from measuring the vertical spacing, D, between adjacent fringes in Fig. 5(b). The brightness level at a point in Fig. 5(c) is proportional to the spacing between a pair of fringe lines nearest to that point. In particular, the larger the distance, the brighter the point. Therefore, the image in Fig. 5(c) is a pitch map showing vertical spacing between adjacent fringes (in the y direction) over the entire area.

Subsequent multiplication of a smoothed, inverse pitch map, which is identical to local fringe density, by $p/2\Delta$ (see Eq. (18)) provides a desired full-field curvature map, as shown in Fig. 5(d). The curvature map enables us to obtain information on the vertical, direct curvature component (κ_{yy}) across a wafer.

Similarly, a pitch map corresponding to the horizontal distance between fringes would provide a map of the shear curvature component, κ_{xy}. In addition, if a horizontal slope map, $\partial f/\partial x$, is used as a starting point, an identical procedure would yield both the κ_{xx} and the κ_{yx} maps. Recalling that $\kappa_{xy} = \kappa_{yx}$, it is evident that both slope interferograms are needed to obtain three independent curvature components, κ_{xx}, κ_{yy} and κ_{xy}, which fully determine the full curvature tensor and thus the full stress distribution on the thin film structure deposited on the Si wafer surface.

4. Results and discussion

4.1. Average curvatures compared to large deformation theory

Fig. 6 shows CGS interferograms for both wafers in two orthogonal principal directions. These principal directions were determined experimentally by rotating the wafer about its center. For conditions in which the deformation is in the geometrically non-linear range, the curvature state is no longer isotropic and different curvatures may

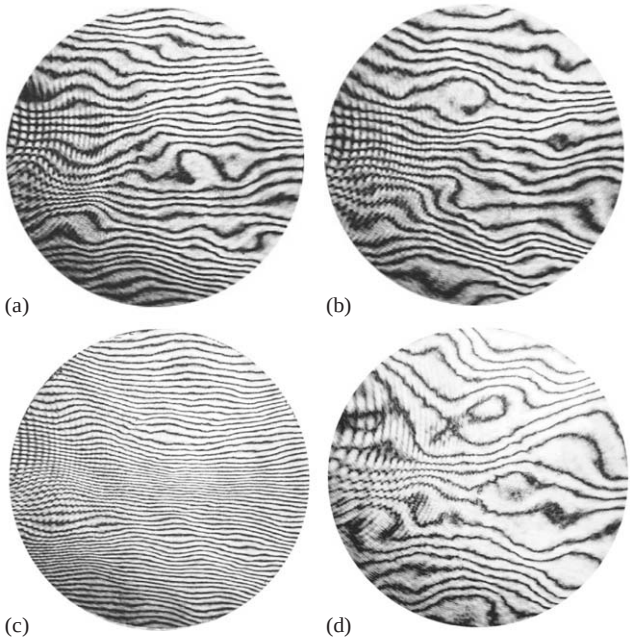

Fig. 6. CGS interferograms of two orthogonal principal directions before bifurcation, (a) and (b), and after bifurcation, (c) and (d), with view field diameter of 52-mm.

exist at different directions. Furthermore, variations of such curvature components may develop from point to point (Finot et al., 1997; Freund, 2000). For the purpose of comparison with large deformation theory, which assumes uniform curvature over the entire region of interest, only central portions (52-mm in diameter), where components of the curvature tensor are essentially constant over our field of view, of the 150-mm (6-in) wafers are presented here. It is observed that, in general, fringes are oriented horizontally (parallel to grating lines), which is an indication that the wafer has been successfully aligned along and across the principal directions. Experimental noise due to the incident laser beam is observed as fringe ripples in the outer regions, and can be removed via subsequent image processing. It is worthwhile to note that from Eqs. (8) and (17), the maximum slope of out-of-plane displacement is $p/2\Delta$ multiplied by the number of fringes in the interferograms. From this calculation, $|\nabla f|_{\max}$ is found to be of the order of 0.02, Fig. 6(c), or less. As a result, the assumptions leading to Eqs. (3) and (18) are satisfied for all practical purposes since $|\nabla f|^2$ is indeed a number much less than unity. This is also consistent with the results of finite element analysis discussed in Freund (2000).

For wafer A, Fig. 6(a) and (b), fringe patterns are approximately the same in two principal directions, which implies that the shape of this wafer remains axisymmetric even in the non-linear deformation regime. For wafer B, however, the number of fringes was found to increase markedly (compared to that of wafer A) in one principal direction, Fig. 6(c), while average fringe density was found to be suppressed in the other direction, Fig. 6(d). It can thus be observed that bifurcation had occurred in wafer B, and that the equilibrium shape changes from a sphere into an ellipsoid. It should be stated here that wafer B features a W film whose thickness is about 2.5 times that of wafer A while deposition conditions were identical.

Average curvatures over the region shown in Fig. 6 are calculated in Eq. (18) from average fringe number density, i.e. total fringe number in the interferogram divided by the diameter of the view field. Variations in local fringe density, which are related to localized curvature, will be discussed in the following section. Average principal curvatures from the CGS measurements are compared to predictions from large deformation theory (Freund, 2000) in Fig. 7. In order to superimpose the experimental points on this figure, the technique used byFinot et al. (1997) was adopted. First, the principal curvatures, in both directions, were obtained by CGS. Then the corresponding stress states were inferred through a numerical model of the exact film–substrate system, which was forced to adopt the same curvatures as measured by CGS. Previous experimental data for the same samples, using laser scanning and grid reflection methods (Finot et al., 1997) are shown for comparison. Curvature and membrane force (or mismatch strain) are normalized into two non-dimensional values defined below (Freund, 2000):

$$\bar{\kappa} = \frac{\kappa D^2}{16 h_s}, \tag{19}$$

$$\bar{\varepsilon}_m = \frac{3\sigma_f h_f D^2}{8\overline{E}_s h_s^3}, \tag{20}$$

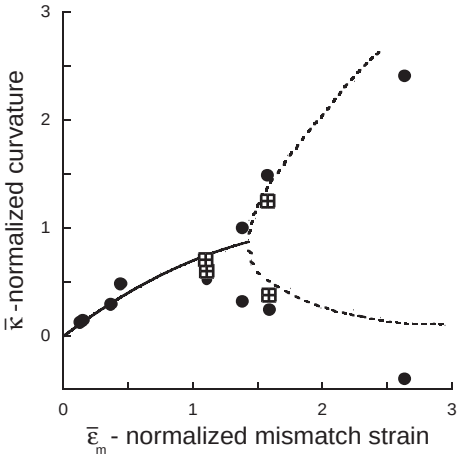

Fig. 7. Comparison of measured normalized curvature versus normalized mismatch strain for Si wafers with W films to analytical prediction based on large deformation by Freund (2000). The filled circles correspond to curvature measurement made by Finot et al. (1997), and the other window symbols denote experimental results from this work.

where $\overline{E_s}$ is 180 GPa for a (100) Si wafer. Agreement between the theory and the experimental measurements is reasonably good for both pre- and post-bifurcation curvatures in the central portion of Si wafers with W film deposits. What is also noteworthy is the relatively good agreement between the various experimental techniques. It is perhaps fortuitous that around the bifurcation point, the curvature radii are of the order of tens of meters. As a result, the relatively low sensitivity of the grid reflection technique did not compromise the comparison. The observed discrepancy may be due to non-uniform curvature evolution, which is not accounted for in theoretical predictions.

In addition to principal curvatures, normal and twist curvature components can be identified at any arbitrary rotation angle θ with respect to principal directions from CGS interferograms. Fig. 8 shows the Mohr's circle representation for pre- and post-bifurcation. Prior to bifurcation (wafer A), a spherical shape is retained with essentially the same principal curvatures in two orthogonal directions. Therefore, Mohr's circle is reduced to a point located along the abscissa. After bifurcation (wafer B), however, one principal curvature is larger than that of the pre-bifurcated wafer, and the other is smaller. For an ellipsoidally curved surface, Mohr's circle is located with its center on the abscissa and its radius defined by Eq. (4). When a wafer is rotated counter-clockwise by θ from the principal direction, twist as well as normal curvature components are found at a location on the circle inclined at 2θ counter-clockwise from the abscissa. The angle ϕ, shown in Fig. 8, is defined by the ratio of twist component to normal curvature as

$$\phi = \arctan\left(\frac{\kappa_{xy}}{\kappa_{\alpha}}\right), \tag{21}$$

where α is either x or y.

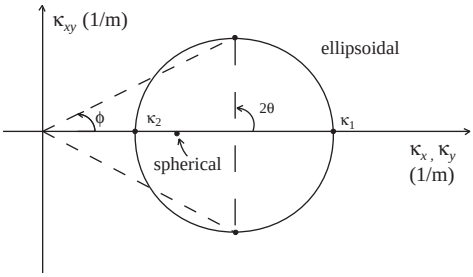

Fig. 8. Schematic of Mohr's circles of spherical wafer shape (before bifurcation) and ellipsoidal shape (after bifurcation) to illustrate curvature components and characteristic angle, ϕ, as rotated by θ from principal direction.

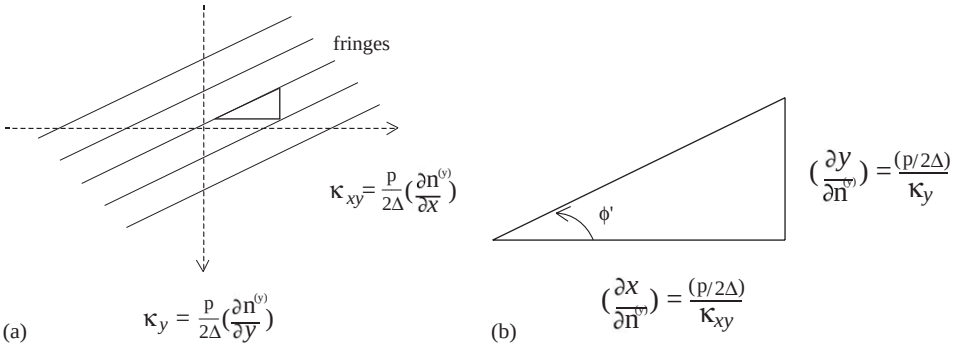

Fig. 9. Schematic of CGS interferrogram as rotated by θ from principal direction (a) measurement of normal and twist curvature components (b) calculation of characteristic angle, ϕ'.

A schematic of the fringe pattern in an off-principal direction is shown in Fig. 9(a). Fringes are no longer parallel to grating lines (horizontal in this experiment), which means there are twist as well as normal components of the curvature tensor. The normal component, κ_y, is measured from the average fringe density along the y-direction. In the same way, average fringe density along the x-direction determines the twist component, κ_{xy}. It can be seen that the orientation of the fringes with respect to the grating lines represents the ratio of twist to normal curvature. As shown in Fig. 9(b), the angle ϕ' is defined in the same form as ϕ in Eq. (21). Therefore, predictions of κ_y (or κ_x), κ_{xy} and ϕ at a rotation angle of θ from Mohr's circle based on two principal curvature values, κ_1 and κ_2, can be compared to measurements from CGS interferograms.

Fig. 10 shows CGS interferograms at $\theta = \pm 45°$, where maximum twist curvatures are expected. When the post-bifurcated wafer (wafer B) is rotated by 45° counter-clockwise ($\theta = +45°$), Fig. 10(a), fringes are oriented with a positive slope from left to right. In contrast, when the wafer is rotated by 45° clockwise ($\theta = -45°$), Fig. 10(b), the fringe

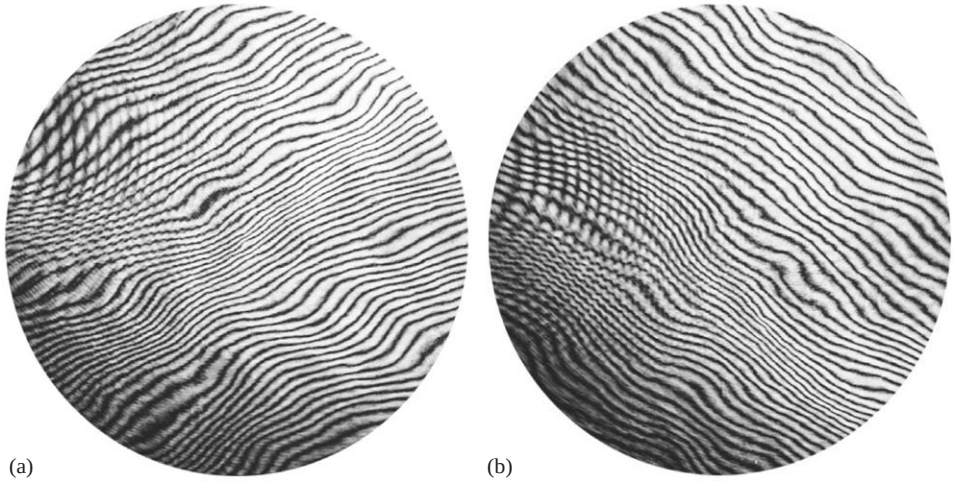

Fig. 10. CGS interferograms (a) $\theta = +45^\circ$ (b) $\theta = -45^\circ$.

Table 1
Comparison between Mohr's circle predictions and CGS interferogram results on normal, twist curvature components and characteristic angle, ϕ, at $\pm 45^\circ$ off principal directions

	From Fig. 6 and Mohr's circle	From Fig. 10	
		$\theta = +45^\circ$	$\theta = -45^\circ$
κ_x or κ_y (1/m)	0.24	0.27	0.23
κ_{xy} (1/m)	0.13	0.13	0.16
ϕ (°)	28	26	33

pattern is distorted in the same general manner but in the opposite sense (negative slope), indicating the onset of substrate twist of opposite sign.

Predictions of κ_y (or κ_x), κ_{xy} and ϕ at $\theta = \pm 45^\circ$ from Mohr's circle and measurements of corresponding values from CGS interferograms are listed in Table 1. The first column is obtained by first recording the principal curvatures from the CGS interferograms of Fig. 6(c) and (d). The Mohr's circle is subsequently used to infer the curvature components at the orientations where maximum twist curvatures occur. The values presented in the second column are directly obtained by measuring curvatures from the interferograms of Fig. 10. In this case the wafer was rotated at $\pm 45^\circ$ to the principal directions. Agreement between these two ways of evaluating curvature components for these in-plane orientations is very good. Such a quantitative agreement is a direct experimental confirmation of the fact that curvature is a tensorial entity which transforms in accordance to the rules described in Section 2.2. In addition, it shows that CGS interferometry is capable of measuring all three curvature components irrespective of the initial choice of wafer orientation and placement.

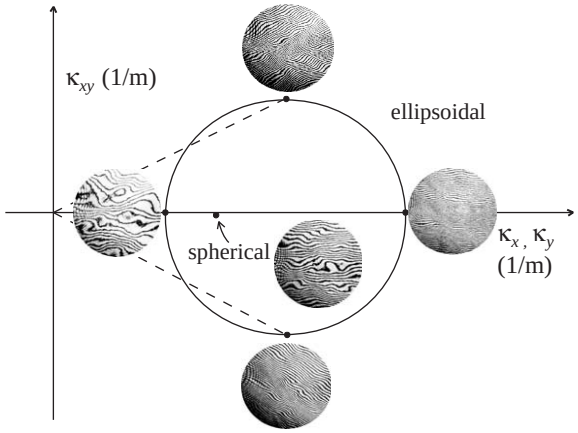

Fig. 11. A series of images showing the correlation of CGS fringe patterns with points on Mohr's circle for curvatures.

Curvature states are summarized on the Mohr's circle with corresponding CGS interferograms as a function of rotation angle for pre- and post-bifurcated wafers in Fig. 11. Prior to bifurcation, all the fringe patterns are essentially independent of rotation angle. This is not surprising since the curvature tensor is essentially isotropic. In contrast, after bifurcation, fringe number increases in one principal direction and decreases in the other for fringes oriented parallel to the grating lines. At $\theta = \pm 45°$, where the maximum twist curvatures occur, fringes have inclination to some degree in opposite sense depending on rotating direction. The numbers and inclination of fringes in these states can be predicted from Mohr's circle; From Eq. (21), fringes at $\theta = \pm 45°$ are approximately parallel to the dotted lines in the Mohr's circle shown in Fig. 11.

4.2. Localized curvatures in a full-field map

Fig. 12 shows the center portion (25-mm × 25-mm) of a CGS interferogram for the post-bifurcated wafer in the principal direction with smaller curvature (a) and the corresponding full field curvature (κ_y) map on a logarithmic scale, which was obtained using image processing analysis (b). In Fig. 12(a) the pitch (or spacing) between adjacent fringes varies from one region to another. Through the image processing techniques outlined in Section 3.2, localized curvatures are calculated based on Eq. (18). In Fig. 12(b), while the region of high fringe density indicates curvature values approximately double the average value (0.10 m^{-1}), the region of low fringe density indicates curvature of less than half this average value. Even in a uniform film, non-uniform curvatures are observed due to variation of intrinsic and/or processing-induced stresses, as well as initial wafer topography. This kind of full-field map enables us to locate area of curvature concentration resulting from such events as initial bare wafer non-planarity, rapid stress gradient, and stress concentration and to identify consequent failure.

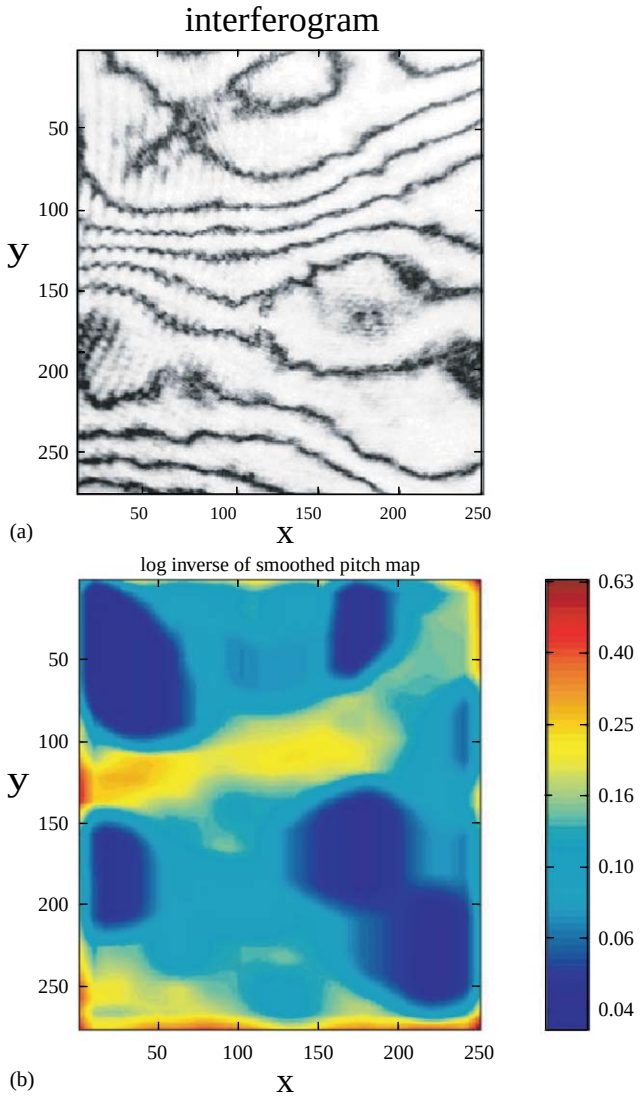

Fig. 12. Construction of full field curvature map (a) CGS interferogram of central portion of wafer (0.1 mm/pixel) (b) corresponding full field curvature contour on logarithm scale (the numbers are converted to linear scale in the index).

5. Conclusions

On the basis of experiments and analyses carried out in the present work for large deformation and bifurcation behavior of W films on Si substrates, the following conclusions

are made:

- The coherent gradient sensing (CGS) technique, which is an optical, full field and vibration-insensitive experimental technique, was used to study large deformation behavior by measuring gradients of out-of-plane displacement of deformed surfaces in the form of surface slope fringes. Since fringe patterns contain information of the wafer surface gradients, all three independent curvature components can be calculated by taking derivatives of the gradient fields. These gradient fields are constructed from two CGS interferograms that correspond to two arbitrarily chosen, but mutually orthogonal directions.
- The measured curvatures in two orthogonal principal directions, the values of which agree reasonably well with analytical predictions based on large deformation theory, clearly show that the equilibrium shape of the wafer changes from a sphere to an ellipsoid upon bifurcation.
- In contrast to the one-dimensional scanning method, which provides only a normal curvature component along the direction of scan, twist (shear) as well as both normal components of curvatures can be obtained by CGS for wafers positioned at an arbitrarily chosen wafer orientation. A classical Mohr's circle representation can be used to identify principal directions and rationalize the evolution of twist curvatures for off-principal orientations.
- Local curvature variation due to non-uniform film stresses can be captured by a full-field curvature map obtained through numerical differentiation of fringe patterns using image processing analysis.

Acknowledgements

This work was supported by the programme on advanced materials for micro- and nano-systems of the Singapore-MIT Alliance (SMA). Helpful discussion of the experimental results with L. B. Freund (Brown U.), D. Owen (Caltech/Oraxion Diagnostics), and S. Omprakash (Caltech/MIT) are gratefully acknowledged.

References

Born, M., Wolf, E., 1986. Principles of Optics. Pergamon Press, New York.

Finot, M., Suresh, S., 1996. Small and large deformation of thick and thin-film multi-layers: effects of layer geometry, plasticity and compositional gradients. J. Mech. Phys. Solids 44, 683–721.

Finot, M., Blech, I.A., Suresh, S., Fujimoto, H., 1997. Large deformation and geometric instability of substrates with thin-film deposits. J. Appl. Phys. 81, 3457–3464.

Floro, J.A., Chason, E., 1996. Measuring Ge segregation by real-time stress monitoring during $Si_{1-x}Ge_x$ molecular beam epitaxial. Appl. Phys. Lett. 69, 3830–3832.

Freund, L.B., 2000. Substrate curvature due to thin film mismatch strain in the nonlinear deformation range. J. Mech. Phys. Solids 48, 1159–1174.

Freund, L.B., Suresh, S., 2003. Thin Film Materials: Stress, Defect Formation and Surface Evolution. Cambridge University Press, Cambridge, U.K.

Giannakopoulos, A.E., Blech, I.A., Suresh, S., 2001. Large deformation of thin films and layered flat panels: effects of gravity. Acta Mater. 49, 3671–3688.

Hyer, M.W., 1981. Some observations on the cured shape of thin unsymmetric laminates. J. Compos. Mater. 15, 175–194.

Lee, H., Rosakis, A.J., Freund, L.B., 2001. Full-field optical measurement of curvatures in ultra-thin-film-substrate systems in the range of geometrically nonlinear deformations. J. Appl. Phys. 89, 6116–6129.

MATLAB Version 6.1, 2001. General Purpose Technical Computing Program. The Mathworks Inc., Natick, MA.

Pan, J.T., Blech, I.A., 1984. In situ measurement of refractory silicides during sintering. J. Appl. Phys. 55, 2874–2880.

Rosakis, A.J., Singh, R.P., Tsuji, Y., Kolawa, E., Moore Jr., N.R., 1998. Full field measurements of curvature using coherent gradient sensing: Application to thin film characterization. Thin Solid Films 325, 42–54.

Salamon, N.J., Masters, C.B., 1995. Bifurcation in isotropic thin film/substrate plates. Int. J. Solid Struct. 32, 473–481.

Stoney, G.G., 1909. The tension of metallic films deposited by electrolysis. Proc. Roy. Soc. London 82, 172–175.